ADVANCED ELECTRONIC MATERIALS
www.advelectronicmat.de

Colossal Tunneling Electroresistance in Co-Planar Polymer Ferroelectric Tunnel Junctions

Manasvi Kumar, Dimitra G. Georgiadou, Akmaral Seitkhan, Kalaivanan Loganathan, Emre Yengel, Hendrik Faber, Dipti Naphade, Aniruddha Basu, Thomas D. Anthopoulos, and Kamal Asadi**

Ferroelectric tunnel junctions (FTJs) are ideal resistance-switching devices due to their deterministic behavior and operation at low voltages. However, FTJs have remained mostly as a scientific curiosity due to three critical issues: lack of rectification in their current-voltage characteristic, small tunneling electroresistance (TER) effect, and absence of a straightforward lithography-based device fabrication method that would allow for their mass production. Co-planar FTJs that are fabricated using wafer-scale adhesion lithography technique are demonstrated, and a bi-stable rectifying behavior with colossal TER approaching 10^6% at room temperature is exhibited. The FTJs are based on poly(vinylidenefluoride-co-trifluoroethylene) [P(VDF-TrFE)], and employ asymmetric co-planar metallic electrodes separated by <20 nm. The tunneling nature of the charge transport is corroborated using Simmons direct tunneling model. The present work is the first demonstration of functional FTJs manufactured via a scalable lithography-based nano-patterning technique and could pave the way to new and exciting memory device concepts.

1. Introduction

Two-terminal resistive switching devices that upon application of an external bias toggle between a low resistance ON- and a high resistance OFF-state, are ideal for memory and synaptic neuromorphic applications.[1–5] Ferroelectric tunnel junctions (FTJs), an extension of polar switch proposed by Esaki et al.,[3] is a metal/ferroelectric/metal junction with the ferroelectric layer being thin enough to allow for quantum mechanical tunneling of the charge carriers from one electrode through the ferroelectric tunnel barrier to the counter electrode. The resistance of the junction, or tunneling electroresistance (TER), switches between two nonvolatile states through the reorientation of polarization of the insulating ferroelectric tunnel barrier.[6–10]

Among the resistance switching devices based on ferroelectric polymers, FTJs are the least successful ones.[5] Polymers based on polyvinylidene fluoride, PVDF, and its random copolymer with trifluoroethylene, P(VDF-TrFE), have been extensively investigated in ferroelectric field-effect transistors (Fe-FETs) and diodes.[11–17] The resistance-switching mechanisms in Fe-FETs and diodes are well understood, and up-scaling has been demonstrated using industrially viable lithography or printing technologies.[18–22] The challenges in upscaling P(VDF-TrFE)-based FTJs are associated with contact formation to soft polymeric ultra-thin films, and the lack of a reproducible and industrially viable fabrication method. Besides the lack of a simple and straightforward lithography-based FTJ fabrication method, the absence of clear rectification in the current–voltage characteristics hampers application of the FTJs as memory elements.[23]

Contact formation on ultra-thin ferroelectric films has proven to be technically very challenging.[24] The community has exclusively focused on out-of-plane vertical stacks of metal/ferroelectric/metal layers.[6–10,25] The critical step in the fabrication of a FTJ is the deposition of the metallic top electrode. Direct vapor deposition of metals such as Au or Pt onto the ultra-thin polymeric layers can easily create local electrical shorts.[26] On the other hand, deposition of reactive metals is not desired because of the creation of an interfacial non-ferroelectric dead-layer.[27,28] Alternatively, FTJs have been realized using scanning probe techniques such as piezoresponse force microscopy (PFM) and conductive atomic force microscopy (C-AFM).[1,5,6,29–32] The probe techniques, however, suffer from poorly defined contact geometry, device area and scalability.[33] For viable FTJ memories, there is still much need for

M. Kumar, Dr. K. Asadi
Max-Planck Institute for Polymer Research
Ackermannweg 10, 55128 Mainz, Germany
E-mail: asadi@mpip-mainz.mpg.de

Dr. D. G. Georgiadou
Department of Physics and Centre for Plastic Electronics
Blackett Laboratory
Imperial College London
Exhibition Road, London SW7 2BW, UK

A. Seitkhan, K. Loganathan, Dr. E. Yengel, Dr. H. Faber, Dr. D. Naphade, Dr. A. Basu, Prof. T. D. Anthopoulos
Division of Physical Sciences and Engineering
King Abdullah University of Science and Technology
Thuwal 23955-6900, Saudi Arabia
E-mail: thomas.anthopoulos@kaust.edu.sa

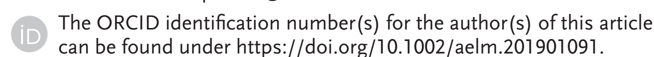
The ORCID identification number(s) for the author(s) of this article can be found under https://doi.org/10.1002/aelm.201901091.

© 2019 The Authors. Published by WILEY-VCH Verlag GmbH & Co. KGaA, Weinheim. This is an open access article under the terms of the Creative Commons Attribution License, which permits use, distribution and reproduction in any medium, provided the original work is properly cited.

DOI: 10.1002/aelm.201901091

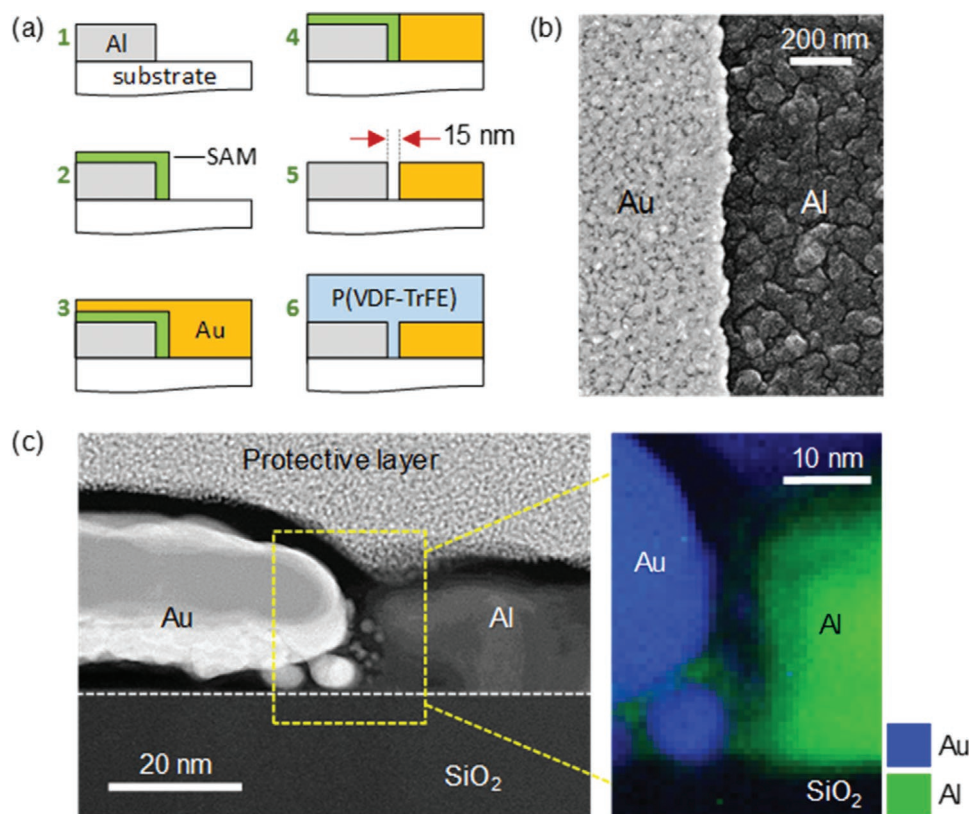

Figure 1. a) Schematic showing the device fabrication using the principle of adhesion lithography for the patterning of nanogap asymmetric Al/Au electrodes (1. Al deposition and photolithography patterning, 2. Self-assembled monolayer (SAM) functionalization of Al, 3. Au deposition, 4. Au removal from SAM-functionalized area of Al, 5. SAM burn off and empty nanogap formation) and finished off with P(VDF-TrFE) layer deposition (6). b) Top view SEM image depicting the Au/Al interface. c) Cross-sectional TEM image of the Au/Al nanogap area with elemental mapping, showing an inter-electrode separation less than 10 nm.

a reliable lithography-based technique that allows reproducible fabrication and enables upscaling and integration.

In-plane devices such as break junctions have been successfully used for the study of tunneling transport through single molecules.[30,34,35] The in-plane configuration has the advantage that the electrodes can be fabricated before deposition of the ferroelectric layer atop. However, techniques like break junctions have low device throughput and are not suited for upscaling.[7,8,36] It has been demonstrated recently that a lithography-based method, namely adhesion lithography (a-Lith), schematically shown in **Figure 1**a, can alleviate the poor scalability issues of the break junctions, and allow for rapid fabrication of nanogap electrodes, with typical gap spacing between 4–10 nm.[33,37] A-Lith has been successfully employed in for the fabrication of nanoscale memristors based on both inorganic and organic semiconductors.[33,37]

Here, we employ a-Lith to fabricate nanogap with asymmetric electrodes and demonstrate FTJs based on the ferroelectric polymer P(VDF-TrFE) that show stable and reproducible giant TER approaching 10^6%; to our knowledge this is the largest reported value to date for metal/polymer/metal FTJs. Asymmetric nanogaps with Al and Au electrodes with spacing of less than 10 nm, Figure 1b–c, are employed for the realization of the FTJs. The resulting FTJ is a non-volatile two-terminal resistive memory with rectifying behavior and shows time-invariance of the tunneling current in the programmed states. We show unambiguously that the current transport through a FTJ is dominated by tunneling that is modulated by ferroelectric polarization of P(VDF-TrFE) in the gap.

2. Demonstration of FTJ

To ensure the successful formation of electrically-isolated nanogaps, we perform current–voltage (I–V) measurements before deposition of the P(VDF-TrFE) layer. Bias is applied to the Au electrode, while the Al electrode is grounded. The bias is swept from 0 to +5 V, to −5 V and back to 0 V. The current for the as-prepared (empty) nanogaps, shown with black symbols in **Figure 2**a, is in the order of 10 pA, and close to the detection limit of our measurement setup. Hence, the Au and Al electrodes are electrically isolated and, thus, reliable nanogaps that are spatially separated have been formed.

Following the demonstration of the isolated electrodes with nanometric gaps, we measure current transport through Au/P(VDF-TrFE)/Al nanogap devices. A 300 nm-thick layer of P(VDF-TrFE) (63-35) (Solvay) is spin-coated at room temperature atop the fabricated nanogaps from 5 wt% cyclopentanone solution.[18] The devices are annealed at 140 °C in a partial vacuum (1 mbar) for 2 h to increase the crystallinity of the P(VDF-TrFE) layer.

 © 2019 The Authors. Published by WILEY-VCH Verlag GmbH & Co. KGaA, Weinheim

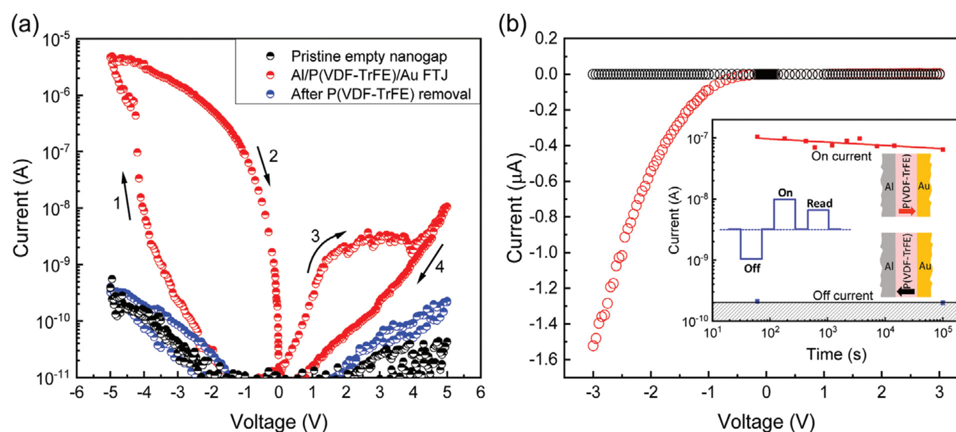

Figure 2. a) I–V characteristics of the tunnel junction. Black symbols show the pristine empty nanogap, prior to deposition of P(VDF-TrFE) layer. Red symbols show the bistable switching behavior of the tunnel junction after deposition of P(VDF-TrFE) polymer. Blue symbols show the I–V of an empty nanogap device after washing off the P(VDF-TrFE) layer. At −3 V, TER ratio is ~10^6%. b) The red and black symbols show the low-voltage I–V curves for the on- and off-states of the Al/P(VDF-TrFE)/Au tunnel junctions for negative and positive polarization of the P(VDF-TrFE) layer, respectively. The I–V shows that FTJ is a bistable rectifying device. The inset shows the program used for retention measurements of both on- and off-states after polarizing the device by applying a voltage pulse of −/+ 5 V and reading at low voltage bias of −3 V.

Piezoelectric force microscopy (PFM) is performed to demonstrate ferroelectricity of the P(VDF-TrFE) layer, as shown in Figure S2, Supporting Information. A writing voltage of +7 V is applied to 7 × 7 μm^2 area, to put P(VDF-TrFE) in negative polarization state. Application of −7 V to a 4 × 4 μm^2 area reverses the polarization. The recorded phase map, Figure S2b, Supporting Information, confirms the complete reversibility of the ferroelectric domains. Moreover, the PFM phase image, Figure S3, Supporting Information, of the polarization map on the nanogap area, unambiguously, proves formation of a good contact between P(VDF-TrFE) and the electrodes.

To electrically characterize the FTJ, bias is applied on the Au electrode and varied from 0 to −5 V, to +5 V and back to 0 V. Figure 2a shows the measured I–V sweep. For the sweep direction from 0 to −5 V, the current is initially in the order of 10 pA. At nearly −2 V, the current begins an exponential rise with increasing |voltage|, and then shows a steep jump at −4 V from several nA to nearly 1 μA, eventually reaching 5 μA at −5 V. Upon back sweeping from −5 to 0 V, the current remains high and follows a different path, exhibiting a hysteretic behavior. During the sweep from 0 to +5 V, in the beginning, the current shows exponential rise with bias up to nearly +2 V. Above +2 V the current saturates, and between +4 and +5 V, the current increases slightly. For the scan direction +5 to 0 V, the current exponentially decreases with the bias. The full I–V loop is hysteretic and shows a bistable rectifying behavior. The junction switches to low-resistance on- and high-resistance off-state at −4 and +4 V, respectively. The spacing between the Au and Al electrodes for the FTJs is less than 10 nm (Figure 1c). Therefore, the electric field at which resistance switching occurs amounts to ≈400 MV/m. The switching electric field coincides with the coercive field that is reported for ultra thin-films of P(VDF-TrFE).[38,39] The occurrence of the resistance switching at electric fields comparable to the coercive field of P(VDF-TrFE) is a strong indication that the modulation of the resistance is due to polarization switching of the P(VDF-TrFE) ferroelectric layer present in the nanogap. To explicitly attribute the measured I–V to polarization switching of P(VDF-TrFE), in the next step we wash away the polymer film from the junction. The current, as shown in Figure 2a, drops down to a value comparable to that of the as-prepared pristine junction, viz. 10 pA.

To demonstrate programmability of the Au/P(VDF-TrFE)/Al junction, pulses of ±5 V are applied for 100 ms to set the junction into high/low-resistance states. The programmed state is subsequently probed either using a voltage sweep between −3 and 3 V or a voltage pulse at ±3 V. As shown in Figure 2b, the Au/(PVDF-TrFE)/Al junction can be programmed into two distinct on- and off-states. In the on-state, the junction shows rectifying behavior, which is highly desired for memory applications.[40–42]

The device shows a colossal TER ratio of 8 × 10^5%, which in combination with rectifying behavior, makes the coplanar FTJs stand out among other devices reported in literature as summarized in **Table 1**. The TER ratio has been obtained from the on- and off-state currents at −3 V which amount to 8 × 10^{-7} A

Table 1. Comparison of the reported TER for P(VDF-TrFE)-based FTJs.

Reference	Device geometry	TER [%]	Rectifying
[6]	C-AFM	80	Yes
[7]	MCB-junction	100	No
[8]	Nanogaps by FIB	189	No
[26]	in-situ FIB -SEM	20	No
[29]	CT-AFM	75 000	–
[30]	In-plane electrodes	–	–
[31]	In-plane electrodes by electromigration	–	–
[32]	STM	–	–
[34]	In-plane electrodes	3200	No
[36]	In-plane electrodes	250	No
[43]	Vertical electrodes	1000	No
[44]	In-plane electrodes	500	No
Present work	Co-planar nanogap by a-lith	800 000	Yes

 © 2019 The Authors. Published by WILEY-VCH Verlag GmbH & Co. KGaA, Weinheim

and 1×10^{-10} A, respectively, and approaches 10^6%. To probe the retention time of the programmed resistive states, a critical parameter for the applications of FTJs, we program the FTJs into the on- and off-states by application of ±5 V pulses, and read the states at −3 V in time. Both the on- and off-states do not show any deterioration for a period longer than 24 h, as shown in inset of Figure 2b.

The work functions of the Au and Al electrodes amount to 4.9 and 4.2 eV, respectively. Therefore, there is a built-in potential, $\Delta\varphi$, of 0.7 eV in the junction in the absence of the external bias. Considering that the nanogap is ≈10 nm, the built-in field amounts to 70 MV m^{-1}. The coercive field at which P(VDF-TrFE) switches is 400 MV m^{-1}, which is nearly six times larger than the built-in field. Therefore, no back switching or depolarization of P(VDF-TrFE) would be expected. Consequently, a long retention time is anticipated and indeed is experimentally measured. The programming and read voltages of, respectively, 5 and 3 V are compatible with today's electronic. The FTJs enable readout at any voltage below the coercive bias. The programming voltage of the FTJ depends on the gap size between the electrodes Hence, upon reducing the gap size, programming voltage drops. Optimization of the nanogap for low voltage operation however is beyond the scope of the present work. Moreover, the FTJs show good cycle endurance upon repeated cycling. As presented in Figure S4, Supporting Information, the TER remains unchanged upon cycling for more than 3000 cycles, which ensure endurance of the nanogap FTJs. The measured cycle endurance is acceptable for the targeted applications of the FTJs, namely as memory element in low-cost/disposable electronics and RFID tags.

In the following we have programmed the device into the on-state and measured the *I–V* sweeps at different temperatures to study the charge transport mechanism in the Au/P(VDF-TrFE)/Al nanogap junction. **Figure 3**a shows temperature dependence of the on-state current sampled at −3 V. We have employed Simmons model[45] as the simplest tunneling model to describe electron tunneling from one metallic contact to another through the P(VDF-TrFE) thin layer. The tunneling current shows a weak quadratic temperature described by[46]

$$J_{T>0K} = J_{0K}\left(1+\frac{1}{6}(\pi\alpha k_B T)^2\right) \quad (1)$$

where $J_{0\,K}$ is the current passing through the junction at 0 K, α is a constant, k_B is Boltzmann constant and T is temperature. Fitting Equation (1) to experimentally measured current, gives $J_{0\,K}$ and α that amount to 2.0×10^{-7} A, and 4.5×10^{21} N.m., respectively. The Au/P(VDF-TrFE)/Al is therefore a ferroelectric tunnel junction.

The current in the on-state depends only on the tunnel barrier heights.[47–49] Following Simmons model[50,51] for tunneling through insulating films with a generalized potential barrier, the current flowing through the junction is

$$J = J_T\left[\bar{\varphi}\exp\left(-C\bar{\varphi}^{1/2}\right)-\left(\bar{\varphi}+qV\right)\exp\left(-C\left(\bar{\varphi}+qV\right)^{1/2}\right)\right] \quad (2)$$

where J_T, C, and $\bar{\varphi}$ are the current pre-factor, tunneling parameter, and the tunnel barrier height at the Fermi level of the electrodes. We note, C is proportional to the electron's effective mass.

Representative *I–V* characteristics of the FTJ at room- (293 K) and low-temperature of 113 K are shown in Figure 3b. Equation (2) describes very well the *I–V* characteristics of the FTJ at reverse bias, as shown in Figure 3b. We have determined the values for J_0, C, and $\bar{\varphi}$ from the fits. Interestingly, all *I–V* curves could be fitted using similar C and $\bar{\varphi}$ of 1.18 ± 0.005 and 2.89 ± 0.02 eV, respectively. The temperature dependence comes from J_T, which is well described by Equation (1).

For the positive bias, that is, when tunneling from the Au electrode, the current can be described with Equation (2) with the same C value but using a different J_0 and $\bar{\varphi}$ of $\approx 4 \times 10^{-9}$ A m^{-2} and 4.2 eV, respectively. Presence of a much larger tunnel barrier of 4.2 eV at the interface between the Au electrode and P(VDF-TrFE) gives much lower current at positive biases, and yield a rectifying behavior in the FTJ. We note that, in the off-state, both forward and reverse bias currents are low and comparable to the leakage (noise) current. Therefore, any attempt to analyze the off-state current, at this point, is prone to wishful interpretations.

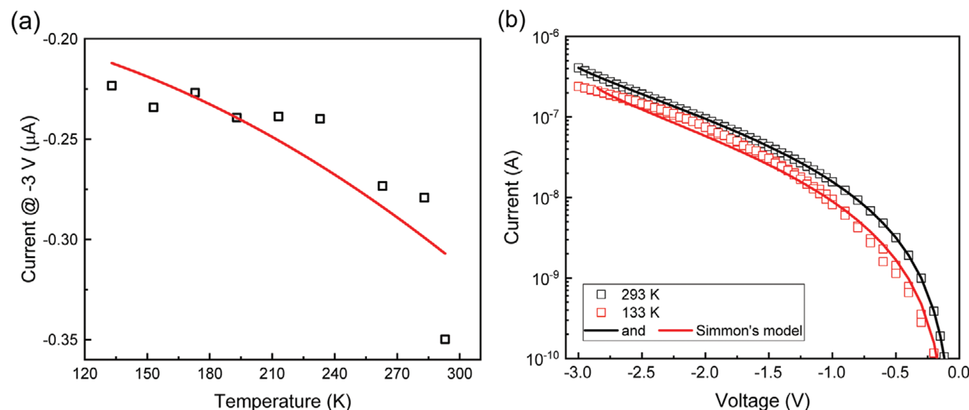

Figure 3. a) Temperature dependence of the on-state current sampled at −3 V. b) Representative *I–V* sweeps at the highest (RT) and lowest measured temperatures of 293 and 133 K. The solid lines in a) and b) are fitted using Equations (1) and (2), respectively.

© 2019 The Authors. Published by WILEY-VCH Verlag GmbH & Co. KGaA, Weinheim

3. Discussion

The choice of Simmons model is due to its simplicity, and obtaining reasonably good fits to experimental data shows its suitability. The Simmons model, considers only elastic electron tunneling, and is valid for low electric fields. The tunneling electrons, provided that they have enough energy, can lose energy through exciting vibrations of the C—H or C—F bonds, which leads to an inelastic tunneling path and an additional contribution to the tunneling current. However, the applied bias of ±3 V is low to activate inelastic processes. Application of more elaborate tunneling models that take for instance charge trapping into account, may produce better fits through introducing more fit parameters. Such models require a knowledge of electron trap density, distribution, and their energy levels, which are lacking for PVDF and P(VDF-TrFE), hence hindering application of such models. We note that the fits in Figure 3b have been obtained using a constant temperature-independent tunnel barrier, $\overline{\varphi}$. Assuming $\overline{\varphi}$ as a floating fit parameter improves the fit quality but reduces the $\overline{\varphi}$ to a meaningless fit parameter.

The energy band diagram of the Al/P(VDF-TrFE)/Au FTJs in its un-polarized pristine state is shown in **Figure 4**a. To draw the band diagram we assumed that the lowest unoccupied molecular orbital (LUMO) of P(VDF-TrFE) lies at 3.5 eV.[52] The work function of Al and Au electrodes have been measured using Kelvin probe and amount to 4.2 and 4.9 eV, respectively. We have included a thin insulating barrier at the Al electrode to account for the presence of the native Al-oxide layer, which is typically ≈1 nm thick. Figure 4b shows the FTJ under negative polarization, at zero bias. Due to the presence of polarization charges, there is a slight distortion in the alignment of the energy levels, particularly of the LUMO of P(VDF-TrFE). We note the thickness of the skin depth for the metal electrode can be disregarded because of its small magnitude, compared to the thickness of the P(VDF-TrFE) layer.[48] Figure 4c, shows the FTJ in the on-state under the reverse bias of −3 V. The ferroelectric polarization is pointing toward the Au electrode. The effective tunnel barrier width is shown with the yellow arrow. Because both the external field and ferroelectric polarization are parallel, under the reverse bias condition, the tunneling barrier width is substantially lowered and the current is high. The forward bias situation is shown in Figure 4d. Ferroelectric polarization and applied external field are anti-parallel. Moreover, the majority of the applied potential is dropped over the P(VDF-TrFE) layer. Therefore, the Al-oxide barrier acts as an extra barrier which blocks charge transport. As a result, the effective tunnel barrier is large and the current under forward bias is substantially lower. Therefore, the presence of the Al-oxide interfacial layer would lead to a rectifying behavior of the junction. The tentative description based on the band diagram is in agreement with the calculated J_0 and $\overline{\varphi}$ for both reverse and forward bias situations.

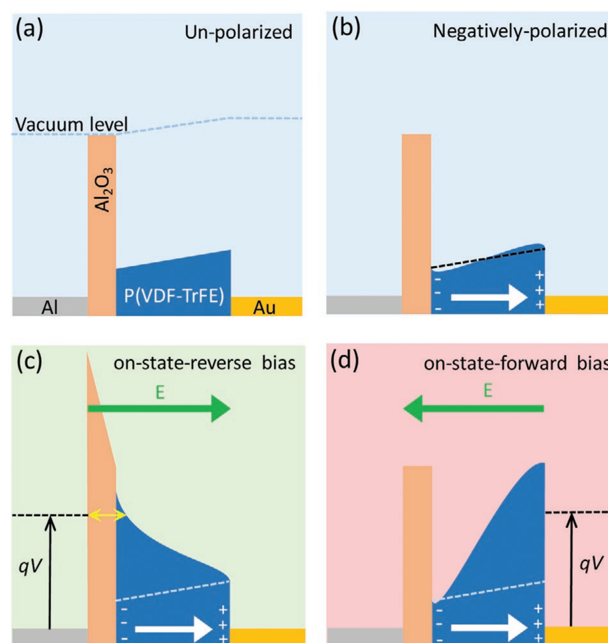

Figure 4. Tentative energy band diagram of Al/P(VDF-TrFE)/Au FTJ at a) pristine unpolarized state, b) negatively polarized on-state at zero bias, with the white arrow indicating the direction of ferroelectric polarization, c) negatively polarized on-state at reverse bias of −3 V with the yellow arrow indicating tunnel barrier width, and d) negatively polarized on-state at forward bias of +3 V. Green arrows indicate direction of electric field.

4. Conclusion

In conclusion, we have demonstrated rectifying FTJs with P(VDF-TrFE) using co-planar nanogap asymmetric electrodes fabricated by adhesion lithography; a simple, scalable and highly cost-effective patterning technique. The FTJs exhibit ferroelectric polarization switching at room temperature and giant TER approaching 10^6%, along with excellent data retention. Analysis of the current-voltage characteristics suggests direct tunneling as the dominant charge transport mechanism across the P(VDF-TrFE) ferroelectric tunnel junction. Barrier modulation at the Al/P(VDF-TrFE) electrode interface is responsible for the observation of giant TER effect in these planar FTJs that have been realized via wafer-scale adhesion lithography. The fabrication technique of the FTJs is a low-cost method that bears the potential for up-scaling and large-scale integration, and paves the way toward an industrially viable memory element for emerging large-area electronics.[53,54]

5. Experimental Section

Nanogap Fabrication by Adhesion Lithography: The nanogap electrodes with asymmetric Al/Au metal contacts are fabricated using a-Lith on silicon wafers (with thermally grown SiO_2). Figure 1a displays the process steps used for the formation of the device with co-planar nanogap electrodes. All Si/SiO_2 wafers are first cleaned by ultrasonication in deionized water, acetone and isopropanol for 10 min and then dried under a stream of dry nitrogen gas. Next, a 40 nm-thick layer of Al is deposited via thermal evaporation in high vacuum (10^{-6} mbar) and subsequently patterned via standard lift-off photolithography and then immersed in an isopropanol solution containing 1 mM Octadecylphosphonic acid (ODPA) (Sigma-Aldrich) for 20 h to form a dense self-assembled monolayer (SAM) atop the native alumina (Al_2O_3) layer. Subsequently the wafers are removed from the SAM solution, rinsed with isopropanol, and then dried/annealed at

© 2019 The Authors. Published by WILEY-VCH Verlag GmbH & Co. KGaA, Weinheim

75 °C on a hotplate for 10 min. After deposition of the second electrode (Au, 80 nm), a thin coating of the commercial adhesive First Contact is applied from solution over the entire sample's surface and left to dry at room temperature for 30 min. The adhesive layer is then manually peeled-off to remove regions of the top Au layer overlapping with the bottom SAM-treated Al electrodes. The resulting patterns consist of co-planar asymmetric electrodes with a nominal inter-electrode gap of ≈10 nm. ODPA is removed from the surface using 10 min UV/O_3 treatment. The adjacent Al/Au electrodes are shown in the top view scanning electron microscopy (SEM) image in Figure 1b, where the presence of a homogeneous interface with nm-scale gap between the two metal electrodes is clearly visible. The nanogap is continuous over large distances as demonstrated by atomic force microscope (AFM) image of the metal electrodes in Figure S1, Supporting Information. The extreme dimensionality of the nanogap can be better visualized in the cross-sectional transmission electron microscope (TEM) image shown in Figure 1c, where short inter-electrode distances <10 nm can be discerned.

Supporting Information

Supporting Information is available from the Wiley Online Library or from the author.

Acknowledgements

M.K. and K.A. acknowledge the financial support of the Max-Planck Institute for Polymer Research and Alexander von Humboldt Foundation (Germany) through the Sofja Kovalevskaja Award, the technical support from H.J. Gutmann. A.S., K.L., E.Y., H.F., D.D., A.B., and T.D.A. acknowledge the King Abdullah University of Science and Technology (KAUST) for financial support. The authors thank Prof. P. W.M. Blom for fruitful discussion.

Conflict of Interest

The authors declare no conflict of interest.

Keywords

ferroelectrics, lithography, piezoelectric force microscopy, polymers, tunnel junctions

Received: October 7, 2019
Revised: December 9, 2019
Published online: December 19, 2019

[1] A. Chanthbouala, V. Garcia, R. O. Cherifi, K. Bouzehouane, S. Fusil, X. Moya, S. Xavier, H. Yamada, C. Deranlot, N. D. Mathur, *Nat. Mater.* **2012**, *11*, 860.
[2] S. H. Jo, T. Chang, I. Ebong, B. B. Bhadviya, P. Mazumder, W. Lu, *Nano Lett.* **2010**, *10*, 1297.
[3] A. L. Esaki, R. Laibowitz, P. Stiles, *IBM Tech. Discl. Bull.* **1971**, *13*, 114.
[4] J. Scott, *Science* **2007**, *315*, 954.
[5] E. Y. Tsymbal, H. Kohlstedt, *Science* **2006**, *313*, 181.
[6] A. Gruverman, D. Wu, H. Lu, Y. Wang, H. Jang, C. Folkman, M. Y. Zhuravlev, D. Felker, M. Rzchowski, C. Eom, *Nano Lett.* **2009**, *9*, 3539.
[7] M. A. Reed, C. Zhou, C. Muller, T. Burgin, J. Tour, *Science* **1997**, *278*, 252.
[8] K. Asadi, P. W. M. Blom, D. M. de Leeuw, *Appl. Phys. Lett.* **2011**, *99*, 053306.
[9] T. Li, W. Hu, D. Zhu, *Adv. Mater.* **2010**, *22*, 286.
[10] A. A. Kornyshev, A. M. Kuznetsov, J. Ulstrup, *Proc. Natl. Acad. Sci. USA* **2006**, *103*, 6799.
[11] J. Wang, B. Liu, X. Zhao, B. Tian, Y. Zou, S. Sun, H. Shen, J. Sun, X. Meng, J. Chu, *Appl. Phys. Lett.* **2014**, *104*, 182907.
[12] H. Qu, W. Yao, T. Garcia, J. Zhang, A. Sorokin, S. Ducharme, P. A. Dowben, V. Fridkin, *Appl. Phys. Lett.* **2003**, *82*, 4322.
[13] Q. Zhang, V. Bharti, X. Zhao, *Science* **1998**, *280*, 2101.
[14] X. Chen, X. Han, Q. D. Shen, *Adv. Electron. Mater.* **2017**, *3*, 1600460.
[15] K. Narayanan Unni, R. de Bettignies, S. Dabos Seignon, J. M. Nunzi, *Appl. Phys. Lett.* **2004**, *85*, 1823.
[16] K. Asadi, D. M. De Leeuw, B. De Boer, P. W. Blom, *Nat. Mater.* **2008**, *7*, 547.
[17] J. J. Brondijk, K. Asadi, P. W. M. Blom, D. M. de Leeuw, *J. Polym. Sci., Part B: Polym. Phys.* **2012**, *50*, 47.
[18] I. Kymissis, C. Dimitrakopoulos, S. Purushothaman, *IEEE Trans. Electron Devices* **2001**, *48*, 1060.
[19] S. Y. Min, T. S. Kim, B. J. Kim, H. Cho, Y. Y. Noh, H. Yang, J. H. Cho, T. W. Lee, *Nat. Commun.* **2013**, *4*, 1773.
[20] K. Fujisaki, H. Koga, Y. Nakajima, M. Nakata, H. Tsuji, T. Yamamoto, T. Kurita, M. Nogi, N. J. Shimidzu, *Adv. Funct. Mater.* **2014**, *24*, 1657.
[21] M. C. Gather, A. Koehnen, A. Falcou, H. Becker, K. Meerholz, *Adv. Funct. Mater.* **2007**, *17*, 191.
[22] L. Ji, Y. F. Chang, B. Fowler, Y. C. Chen, T. M. Tsai, K. C. Chang, M. C. Chen, T. C. Chang, S. M. Sze, E. T. Yu, *Nano Lett.*. **2014**, *14*, 813.
[23] J. Semple, G. Wyatt-Moon, D. G. Georgiadou, M. A. McLachlan, T. D. Anthopoulos, *IEEE Trans. Electron Devices* **2017**, *64*, 1973.
[24] Y. Kim, K. Y. Lee, S. K. Hwang, C. Park, S. W. Kim, J. Cho, *Adv. Funct. Mater.* **2014**, *24*, 6262.
[25] J. Semple, D. G. Georgiadou, G. Wyatt-Moon, M. Yoon, A. Seitkhan, E. Yengel, S. Rossbauer, F. Bottacchi, M. A. McLachlan, D. D. C. Bradley, T. D. Anthopoulos, *npj Flexible Electron.* **2018**, *2*, Article number: 18.
[26] K. Jung, Y. Kim, W. Jung, H. Im, B. Park, J. Hong, J. Lee, J. Park, J. K. Lee, *Appl. Phys. Lett.* **2010**, *97*, 233509.
[27] Y. Wang, M. K. Niranjan, K. Janicka, J. P. Velev, M. Y. Zhuravlev, S. Jaswal, E. Y. Tsymbal, *Phys. Rev. B* **2010**, *82*, 094114.
[28] M. Li, I. Katsouras, K. Asadi, P. W. M. Blom, D. M. de Leeuw, *Appl. Phys. Lett.* **2013**, *103*, 072903.
[29] V. Garcia, S. Fusil, K. Bouzehouane, S. Enouz-Vedrenne, N. D. Mathur, A. Barthelemy, M. Bibes, *Nature* **2009**, *460*, 81.
[30] Y. Kashimura, H. Nakashima, K. Furukawa, K. Torimitsu, *Thin Solid Films* **2003**, *438-439*, 317.
[31] D. E. Johnston, D. R. Strachan, A. C. Johnson, *Nano Lett.* **2007**, *7*, 2774.
[32] L. Venkataraman, J. E. Klare, I. W. Tam, C. Nuckolls, M. S. Hybertsen, M. L. Steigerwald, *Nano Lett.* **2006**, *6*, 458.
[33] D. J. Beesley, J. Semple, L. K. Jagadamma, A. Amassian, M. A. McLachlan, T. D. Anthopoulos, *Nat. Commun.* **2014**, *5*, ncomms4933.
[34] L. Sun, S. Chin, E. Marx, K. Curtis, N. Greenham, C. Ford, *Nanotechnology* **2005**, *16*, 631.
[35] V. Dubois, S. N. Raja, P. Gehring, S. Caneva, H. S. J. van der Zant, F. Niklaus, G. Stemme, *Nat. Commun.* **2018**, *9*, Article number: 3433.
[36] S. Strobel, S. Harrer, G. Penso Blanco, G. Scarpa, G. Abstreiter, P. Lugli, M. Tornow, *Small* **2009**, *5*, 579.
[37] J. Semple, S. Rossbauer, T. D. Anthopoulos, *ACS Appl. Mater. Interfaces* **2016**, *8*, 23167.

© 2019 The Authors. Published by WILEY-VCH Verlag GmbH & Co. KGaA, Weinheim

[38] S. Ducharme, V. Fridkin, A. Bune, S. Palto, L. Blinov, N. Petukhova, S. Yudin, *Phys. Rev. Lett.* **2000**, *84*, 175.
[39] M. Li, I. Katsouras, K. Asadi, P. W. Blom, D. M. de Leeuw, *Appl. Phys. Lett.* **2013**, *103*, 072903.
[40] M. Kumar, H. Sharifi Dehsari, S. Anwar, K. Asadi, *Appl. Phys. Lett.* **2018**, *112*, 123302.
[41] M. Ghittorelli, T. Lenz, H. S. Dehsari, D. Zhao, K. Asadi, P. W. Blom, Z. M. Kovács-Vajna, D. M. De Leeuw, F. Torricelli, *Nat. Commun.* **2017**, *8*, 15741.
[42] H. Sharifi Dehsari, M. Kumar, M. Ghittorelli, G. Glasser, T. Lenz, D. M. de Leeuw, F. Torricelli, K. Asadi, *Appl. Phys. Lett.* **2018**, *113*, 093302.
[43] K. Asadi, M. Li, K. N. Stingelin, P. W. M. Blom, D. M. de Leeuw, *Appl. Phys. Lett.* **2010**, *97*, 193308.
[44] B. B. Tian, J. L. Wang, S. Fusil, Y Liu, X. L. Zhao, S. Sun, H. Shen, C. G. Duan, M. Bibes, A. Barthélémy, B. Dkhil, V. Garcia, X. J. Meng, J. H. Chu*Nat. Commun.* **2016**, *7*, 11502.
[45] J. G. Simmons, *J. Appl. Phys.* **1964**, *35*, 2655.
[46] R. Stratton, *J. Phys. Chem. Solids* **1962**, *23*, 1177.
[47] A. Chanthbouala, A. Crassous, V. Garcia, K. Bouzehouane, S. Fusil, X. Moya, J. Allibe, B. Dlubak, J. Grollier, S. Xavier, *Nat. Nanotechnol.* **2012**, *7*, 101.
[48] H. Kohlstedt, N. Pertsev, J. R. Contreras, R. Waser, *Phys. Rev. B* **2005**, *72*, 125341.
[49] P. Maksymovych, S. Jesse, P. Yu, R. Ramesh, A. P. Baddorf, S. V. Kalinin, *Science* **2009**, *324*, 1421.
[50] K. C. Kao, W. Hwang, *Electrical Transport in Solids*. International series in the science of the Solid State, Pergamon Press **1981**.
[51] J. Simmons, *J. Appl. Phys.* **1963**, *34*, 1973.
[52] A. N. Hanna, U. S. Bhansali, M. Khan, H. N. Alshareef, *Org. Electron.* **2014**, *15*, 22.
[53] M. Gajek, M. Bibes, S. Fusil, K. Bouzehouane, J. Fontcuberta, A. Barthelemy, A. Fert, *Nat. Mater.* **2007**, *6*, 296.
[54] H. Mirhosseini, I. Maznichenko, S. Abdelouahed, S. Ostanin, A. Ernst, I. Mertig, J. Henk, *Phys. Rev. B* **2010**, *81*, 073406.
[55] D. Y. Kusuma, P. S. Lee, *Adv. Mater.* **2012**, *24*, 4163.

© 2019 The Authors. Published by WILEY-VCH Verlag GmbH & Co. KGaA, Weinheim